Journal of Turbomachinery. Received September 09, 2019;
Accepted manuscript posted October 17, 2019. doi:10.1115/1.4045272

ASME Journal of Turbomachinery

The Influence of Fan Root Flow on the Aerodynamic of a Low-Pressure Compressor Transition Duct

Walker, A Duncan*
Senior Lecturer in Applied Aerodynamics,
Department of Aeronautical and Automotive Engineering,
Loughborough University, Loughborough, Leicestershire, LE11 3TU, UK.
A.D.Walker@lboro.ac.uk

Mariah, Ian
Research Associate,
Department of Aeronautical and Automotive Engineering,
Loughborough University, Loughborough, Leicestershire, LE11 3TU, UK.
I.Mariah@lboro.ac.uk

Tsakmakidou, Dimitra
Research Student,
Department of Aeronautical and Automotive Engineering,
Loughborough University, Loughborough, Leicestershire, LE11 3TU, UK.
D.Tsakmakidou@lboro.ac.uk

Vadhvana, Hiren
Masters Student
Department of Aeronautical and Automotive Engineering,
Loughborough University, Loughborough, Leicestershire, LE11 3TU, UK.
Hiren.Vadhvana@rolls-royce.com

Hall, Chris
Compressor Specialist
Rolls-Royce plc.
PO Box 31, Derby, DE24 8BJ, UK
Chris.Hall@Rolls-Royce.com

*corresponding author

Journal of Turbomachinery. Received September 09, 2019;
Accepted manuscript posted October 17, 2019. doi:10.1115/1.4045272

ABSTRACT

To reduce fuel-burn and emissions there is a drive towards higher bypass ratio and smaller high-pressure ratio core engines. This makes the design of the ducts connecting compressor spools more challenging as the higher radius change increases aerodynamic loading. This is exacerbated at inlet to the engine core by fan root flow which is characterized by a hub-low pressure profile and large secondary flow structures. Additionally, shorter, lighter nacelles mean that the intake may not provide a uniform inlet flow when the aircraft is at an angle of attack or subject to cross winds. Such inlet distortion can further degrade the flow entering the engine. A combination of experiments and CFD have been used to examine the effects on the aerodynamics of an engine section splitter (ESS) and transition duct designed to feed the low-pressure spool of a high bypass ratio turbofan. A test facility incorporating a 1½ stage axial compressor was used to compare system performance for a flat rotor exit profile to one with a hub deficient flow. Validated RANS CFD was then used to further investigate the effects of increased inlet boundary layer thickness and bulk swirl distortion at rotor inlet. These changes were seen to have a surprisingly small effect on the flow at duct exit. However, increased secondary flows were observed which degraded the performance of the ESS and significantly increased loss. Nevertheless, the enhanced mixing delayed separation in the duct suggesting that overall the design was reasonably robust albeit with increased system loss.

INTRODUCTION

In a multi-spool compression system, the diameter of each spool reduces as the air density increases. Consequently, the annular transition ducts connecting spools generally take the form of an S-shape. However, the curvature in these ducts makes them prone to flow separation which must be avoided as it will compromise performance. There has been large amount of work studying the complex flow in annular S-shaped ducts which develops under the combined influence of pressure gradients and streamline curvature. For example, Britchford [1], Bailey [2], Britchford et al. [3-5], Bailey and Carrotte [6], Bailey et al. [7] studied the fundamental aerodynamics and the effect of compressor generated inlet conditions. Additionally, Ortiz-Duenas et al. [8], Barker et al. [9,10], Karakasis et al. [11], and Walker et al. [12-14] studied more aggressive ducts and improved integration with the compression system.

Walker et al. [14] summarized the factors affecting the aerodynamic loading in S-shaped ducts including duct geometry, curvature, boundary conditions etc. With reference to Fig. 1 the radial pressure gradients which exist across the two bends give rise to an adverse streamwise pressure gradient on the hub. This makes the flow in the duct prone to separation in the second bend on the hub wall. The severity of the aerodynamic loading is therefore a function of the duct area ratio (A2/A1), non-dimensional length (L/h1), and non-dimensional radius change ($\Delta R/L$). An upstream compressor will also have an important effect on performance of an S-shaped duct. Bailey et al. [2] and Karakasis et al. [11] measured a notable increase in duct loss due to the presence of compressor generated inlet conditions. However, Britchford [1]

reported that the increased turbulent mixing is also beneficial as it promotes the transfer of higher momentum core flow into the boundary layers thereby delaying separation.

Importantly, all the studies mentioned above examined the duct connecting the intermediate-pressure (IP) compressor to the high-pressure (HP) compressor. However, the duct positioned between the low pressure (LP) fan and the IP compressor (see Fig. 2) has some notable differences which will affect aerodynamic loading and performance. For example, the drive towards very high bypass ratios and geared architectures means that the non-dimensional radius change, and hence aerodynamic loading, in the LP-IP duct can be significantly different to an IP-HP duct. Additionally, the aerodynamics of the LP fan root flow is noticeably different to that at exit to an IP compressor (see for example Zamboni and Xu [15]). Long chord fan blades which rotate relatively slowly at the hub will generate a hub-low total pressure profile compared to a generally flatter IP compressor exit profile. Furthermore, the long chord at the fan root will also generate large secondary flow structures which rotate with the fan and subsequently impinge on the engine section stator (ESS). Finally, the LP fan is often subjected to inlet distortions which can further affect the flow entering the LP-IP duct. Inlet distortions can take the form of increased boundary layer thickness and/or changes in inlet swirl. These distortions are generated by aircraft incidence effects, nacelle scarfing (for noise shielding), gusts and side winds and the current trend for shorter, lighter nacelles will exacerbate this (see, for example Peters et al. [16] who discuss the use of ultra-short nacelles).

SCOPE

The main objectives of the current paper to investigate the effects of the LP fan root flow on the aerodynamics of the ESS and LP-IP compressor transition duct. Specifically:

1. To experimentally examine the effect of a hub-low rotor profile on the aerodynamics of an engine represented ESS and LP-HP compressor transition duct.
2. To generate a validated CFD model and use it to further examine the effect of (i) increasing the hub deficit at inlet and (ii) inlet swirl distortion at rotor inlet.

DUCT GEOMETRY AND TEST CONFIGURATIONS

The datum geometry used here is representative of the duct connecting an LP fan to the IP compressor. The geometry was taken from the Integrated Core Technologies (iCORE) Project which is a collaborative research program lead by Rolls-Royce plc. and funded by the Aerospace Technology Institute. A schematic of the duct is shown in Fig. 3 where it is compared to the LU2 duct used in the previous work of Walker et al. [13]. Although the LU2 duct was designed to be representative of an aggressive IP-HP compressor transition duct the comparison serves to illustrates that the iCORE duct has lower aerodynamic loading in terms of non-dimensional radius change and area ratio. The loading for the iCORE LP-IP duct is more a function of the fan hub profile and the long chord outlet guide vane (OGV) or engine stator splitter (ESS). This component cannot always be aerodynamically optimal. The ESS requires additional thickness and

chord for structural reasons as it must transfer engine loads across the main gas path. The ESS may also need increased physical thickness to allow passage of warm air for anti-icing.

Experimental Test Facility

All experimental data were obtained on the low speed test facility used by Walker et al. [12-14] to investigate IP-HP ducts. The facility (Fig. 4) is operated at nominally atmospheric conditions with air drawn into a large inlet plenum, above the vertically mounted test rig, before passing through an inlet flare and honeycomb flow straightener. The air then accelerates over a bell-mouth intake section prior to passing into the test section which comprises a single stage axial compressor with inlet guide vanes (IGV) providing 10° of pre-swirl, a rotor and engine representative ESS upstream of the S-shape duct. The mean radius at rotor inlet is 320.1mm with a passage height of 71.1mm (h_1). The rotor was operated at a fixed non-dimensional mass flow condition ($m\sqrt{(RT)}/AP$) and speed ($(N\pi D/\sqrt{(\gamma RT)}$) corresponding to a design flow co-efficient (V_a/U_{blade}) of $\phi = 0.55$, a work coefficient ($\Delta H/U_{blade}^2$) of $\psi = 0.4$ giving a mass flow of approximately 6kgs^{-1}. This resulted in an ESS Reynolds number in excess of 2.0 x 10^5 which is sufficiently high to avoid any transitional effects (Cumpsty [17]). Coupled with the relatively high levels of turbulence (>3%) generated by the rotor, the wake mixing within the downstream duct is well represented. The engine representative, structural ESS have an aspect ratio close to 0.7 and turn the flow through approximately 30°. Downstream of the S-duct there is a settling length of ~3.5 duct heights before the flow passes into a sub floor plenum and

through a centrifugal fan, exhausting to atmosphere. The centrifugal fan is used to ensure that the compressor is maintained on the desired operating condition.

Test Configurations

For the data presented herein two different rotor configurations were employed:

1. Phase 1 – pre-existing rotor from the work of Walker et al. [13] which had a nominally flat total pressure profile, broadly representative of a typical IP compressor exit.
2. Phase 2 – new rotor with a hub-low total pressure profile more representative of flow at the LP fan root.

Instrumentation, Data Reduction, Analysis and Errors

Information on the mean flow field was obtained using 1.75mm diameter miniature five-hole pressure probes suitably calibrated and employed in a non-nulled mode (Wray and Carrotte[18]). For the planes shown in Fig. 5 area traverses can be performed corresponding to one repeatable ESS space consisting typically of 21 radial and 31 circumferential points, clustered in regions to capture the boundary layer and wake flow. All measurements were corrected to ISO standard day conditions and the velocities were measured in a local co-ordinate system (Fig. 6). Typically, data are presented in this local format since it enables the development of the flow within the duct to be more easily understood. The 5-hole probe area traverses provided local total and static pressures in addition to the velocity vector. Therefore, at a given plane, spatially averaged values can

be obtained through suitable averaging techniques. The spatially averaged velocity normal to the traverse plane ($\overline{U}$) was obtained by area weighting the individual values while the total pressure ($\tilde{P}$) was mass weighted (as discussed by Klein [19]) such that:

$$\tilde{P} = \tilde{p} + \alpha \frac{1}{2}\rho \overline{U}^2 \text{ and } \alpha = \frac{1}{A}\int^A \left(\frac{U}{\overline{U}}\right)^3 dA$$

where α is the kinetic energy coefficient and compares the kinetic energy flux of the actual profile to a uniform profile with the same mass flow. Note that all data presented herein are for a low-speed, incompressible, isothermal flow; this approach is not valid for compressible flows. Subsequently, Changes in the spatially averaged total pressure between any two planes can then be expressed in terms of a total pressure loss (λ) with the change in pressures being non-dimensionless by a suitable reference dynamic pressure.

$$\lambda = \frac{\tilde{P}_1 - \tilde{P}_2}{\tilde{P}_1 - \tilde{p}_1} = \frac{\tilde{P}_1 - \tilde{P}_2}{(\alpha \frac{1}{2}\rho \overline{U}^2)_1}$$

The general accuracy of the rig hub and casing dimensions was measured, typically, to be of order 0.1mm and at each traverse plane the traverse height was also measured and found to be within 0.2% of that specified. The positional accuracy of the 5-hole pressure probe was within 0.1mm radially and 0.1° circumferentially and the pressures measured were estimated to be accurate to within 1%. The total velocity of the flow was obtained from the dynamic pressure, and hence the accuracy of the local velocities was within ±0.5%. While the pitch angle of the flow was determined from the calibration of the probe, additional errors in yaw angle could arise associated with the ability of the user to align the probe with the rig centreline. It is estimated that this could be set to within 1°,

Journal of Turbomachinery. Received September 09, 2019;
Accepted manuscript posted October 17, 2019. doi:10.1115/1.4045272

and this level of accuracy was reflected in the measured swirl angles and circumferential component of velocity. In addition to the errors associated with the local measurements it was determined that the mass weighted total and static pressures at a given traverse plane were repeatable to better than 10Pa. The calculated mass flows at each traverse plane, derived from the velocity measurements, were all within 2.5% of each other.

EXPERIMENTAL RESULTS AND DISCUSSION

Rotor Exit (X2)

Rotor exit velocity contours and circumferentially averaged profiles are shown in Fig. 7 and 8. They illustrate the relatively flat pressure distribution of the Phase 1 rotor in comparison to the Phase 2 rotor which was designed to have a significant total pressure deficit at the hub. With the static pressure profile nominally unchanged the hub deficit is also seen in the velocity component normal to the plane. Additionally, this results in notable change in the radial distribution of tangential velocity although the swirl angle profiles are comparable and the incidence onto the ESS is therefore nominally unchanged. Note that the swirl angle is plotted relative to the value at mid passage height ($\theta_{0.5}$). The exit swirl is approximately ~1° higher for the Phase 2 rotor but it must be noted that this is close to the measurement accuracy of the five-hole probes. Note also that the circumferential variations seen in the contours result from a combination of the residual wakes from the upstream IGV and the potential field from downstream ESS.

Flow Field Development (A-H)

ESS exit contours and circumferentially averaged profiles are shown in Fig. 9 and 10. The diffusion through the ESS increases the hub deficit and consequently the inboard wake structure is noticeably different. The loss core has increased in size which is consistent with the low momentum end-wall fluid rolling up onto the vane surface. This generally indicates an increased aerodynamic loading and that the vane has moved closer to stall with the hub low Phase 2 rotor. Nevertheless, the swirl profiles show that the ESS still performs the same level of turning.

The development of the total pressure and normal velocity profiles are shown in Fig. 11. The bias generated by the hub low rotor exit profile clearly persists throughout the duct and the average profiles show a larger momentum deficit along the hub wall suggesting that the duct has moved closer to separation. Selected normal velocity contours shown in Fig. 12 and are useful in understanding the development and effect of the ESS wake. The ESS extend though the first bend of the duct such that at plane B the radial pressure gradient due to turning is small. This contrasts with previous studies (Walker et al. [12-14]) where the OGV wakes have been subject to a strong pressure gradient which drives the low momentum wake fluid into the inner wall. This generates a pair of counter rotating vortices but also serves to re-energizes the inner wall boundary. These vortex structures are not seen in the iCORE duct and the ESS wakes are subjected to a streamwise adverse pressure gradient and, in the second bend, an outboard pressure gradient. Although the outer portion of the wakes mix out through the action of shear, the streamwise pressure gradient cause the loss core to grow.

Consequently, the development of the duct flow is more sensitive to the wake structure issuing from the ESS. This is most evident at plane H where the larger ESS secondary flow structure generated by the hub-low phase 2 rotor is still clearly visible. This feature is not present with the nominally flat rotor exit profile of the Phase 1 rotor. In terms of aerodynamic loading the adverse pressure gradient which acts along the inner wall means that an S-duct is most prone to flow separation on the hub at plane E. This is evident in the low velocity regions seen in Fig. 12. However, despite the hub low inlet profile and the differences in ESS wake structure between the two rotor profiles, the depth of these low velocity regions remains similar. Although the radial profiles suggest that duct may have moved closer to separation the contours suggest that locally the effect is not as large. This is a consequence of the enhanced mixing caused by the larger wake structures which transports mainstream momentum into the hub boundary layer.

The development of the total pressure loss coefficient (with respect to rotor exit) is plotted in Fig. 13. Across the ESS the loss is similar despite the marginally larger wake structure generated with the Phase 2 rotor. However, this does produce a larger mixing loss downstream of the ESS and, subsequently, there is a ~12% increase in loss from rotor exit to duct exit for the hub low rotor exit profile (Phase 2).

NUMERICAL METHODOLOGY

The CFD solutions were all computed using a development of the methodology validated by Barker et al. [9, 10] and Walker et al. [12-14]. These previous studies predicted the duct flow only but here both the ESS and the rotor were included in the

domain. The CFD model was based on the experimental geometry but simplified to a 7.5° repeatable sector. Solution of the RANS equations was achieved using ANSYS Fluent (v18.2) with a Reynolds Stress turbulence model. It was found [9, 10, 12-14] that this higher order model is required to capture the effects of curvature. ANSYS TurboGrid was used to generate an O-H mesh. The ESS and duct domain had approximately 80 radial, 46 circumferential and 550 streamwise cells giving a total cell count close to 1.4 million. The rotor domain comprised of 0.4 million cells with a resolution of 80 x 40 x 106. A rotor tip gap equal to 1% of the blade height was modelled with 13 cells. A mixing plane was employed between the rotational and stationary domains. Near wall cells were sized to ensure wall y+ values in the range 30-130 and hence applicable to a wall function approach. It was found that Fluent non-equilibrium wall function produced the best match to the experimental data. Note that a low y+ strategy was also examined but Barker et al. [9, 10] found this provided no notable increase in accuracy but added significant numerical cost. Inlet conditions were taken directly from the experimental measurements. Velocity data were taken from five-hole probe measurements presented early and turbulence data from hot-wire measurements (not shown).

Validation

Fig. 14 compares measured and predicted profiles of total pressure and swirl angle at rotor exit (X2). The data show remarkably good agreement although there is some discrepancy at ~90% span. This can be attributed to modelling of the tip leakage flows. The flow physics in this region are challenging for a steady solver and it is also difficult to

achieve adequate mesh resolution whilst maintaining the required near wall strategy (y+ > 30-130). Nevertheless, the CFD model accurately predicts the bulk pressure and swirl profiles.

Comparing Fig. 14 and 15 with Fig. 9 and 12 the predicted data also show good agreement in the development of the velocity through the ESS and duct. At ESS exit, plane A, the bulk flow features are well represented as are the ESS secondary flow structures. The main difference at plane A is the IGV wake which is still evident in the experimental data but not modelled in the CFD. The subtle differences seen at plane A persist through the duct, but the size and strength of the main features are still well captured. For example, at plane E the low velocity region on the hub wall matches well. The flow is most susceptible to separation at plane E due to the adverse pressure gradient which acts along the inner wall. It is important that the CFD predicts the likelihood of separation. Similarly, at duct exit, plane H, the boundary layer depth, level of wake mixing and general uniformity are all well represented; this represents the flow passed to the downstream compressor and it is again important the CFD captures this. The predicted loss development, shown in Fig. 16, also shows reasonably good agreement with the experimental data. The ESS loss is comparable although the duct loss is slightly underpredicted. Nevertheless, the model is sufficiently validated to be used for further investigation of the ESS and duct aerodynamics.

NUMERICAL RESULTS AND DISCUSSION

Increased Inlet Boundary Layer

To assess the effect of an increased hub boundary layer the profile shown in Fig. 17 was applied to the CFD inlet upstream of the Phase 2 rotor. With reference to the original rig inlet profile the mass flow was maintained which results in an increase in the velocity in the outboard portion. Additionally, to maintain consistency with the original inlet condition the radial profile of swirl angle was maintained. Radial equilibrium dictates that the pressure profiles will also then be adjusted by the CFD, but this is a secondary effect in comparison to the increased momentum deficit for the first 40% of the span.

Predicted normal velocity contours at rotor exit (X2) are shown in Fig. 18. These are plotted in the rotating frame of reference to better highlight changes to the rotor wake structure. The bulk flow pattern is similar for both inlet conditions but, importantly, an increased secondary flow structure can be seen at approximately 30% span. Although this will be circumferentially averaged in the stationary frame of reference the effect on the ESS flow can be seen in Fig. 19. Comparing the normal velocity contours at ESS exit for the two inlet profiles shows smaller differences than perhaps would be expected. A general outer bias remains but the inner wall boundary layer is unchanged. The most obvious difference is the increased size of the wake structure at 25% span which is clearly a function of the structure generated in the rotor. Interestingly though, at plane E (Fig. 20) the low velocity region on the hub wall is reduced. This may seem somewhat counterintuitive; despite the increased momentum deficit at inlet the hub flow is further

from separation at plane E. This is due to the additional mixing of the larger ESS wake structure which entrains more higher momentum mainstream flow into the boundary layer thereby re-energising it. Consequently, the flow at duct exit (Fig. 21) shows little difference other than a slightly increased outboard bias for the inlet condition with an increased hub boundary layer. This is also reflected in the predicted development of the total pressure loss coefficient (from rotor exit) shown in Fig. 22. There is slight increase in predicted loss over the ESS row and a slightly increased duct loss (5%) due to the additional mixing of the ESS wake structure.

Inlet Swirl Distortion

The effect of inlet swirl distortion was assessed by altering the bulk swirl at inlet to the Phase 2 rotor -10° to +14° in steps of 2°. This is a larger variation than normally expected due to aircraft incidence effects but coupled with the possible effects of side winds and gusts the higher values could potentially well be realised. The biggest effect of changing the inlet swirl is a shift in the rotor exit swirl or, in essence, a change in incidence onto the ESS. This is illustrated in Fig. 23 which shows circumferentially averaged swirl angles profiles at rotor exit for ±4° and ±10°. The data suggest that the resultant ESS incidence is offset by approximately half that of the offset in inlet swirl. A negative swirl offset has only a small effect on the ESS exit flow structures (Fig. 24). However, a positive offset notably increases the inboard wake structure which elongates and moves outboard. This also presents a blockage which causes the bulk flow to migrate outboard. Surface streamlines in Fig. 25 show the source of this is a

separation on the suction surface which grows and moves outboard with increasing positive swirl offset.

As before, the increased wake structure at ESS does not necessarily mean the duct becomes more prone to flow separation. In fact, the opposite is again observed in Fig. 26 at plane E. The outboard bias remains broadly similar in all cases but there are clear changes to the low velocity region near the hub wall. In an opposite sense to what is observed at ESS exit this increases at negative swirl offset and decreases at positive swirl offset. Again, this is a function of the increased mixing generated by the ESS wake which entrains higher momentum flow into the hub boundary layer. The flow at duct exit (Fig. 27) again, therefore, shows only minor differences with only a slightly higher level of non-uniformity at positive swirl offset.

The loss coefficient (from rotor exit) is plotted to plane A, E and H, as a function of inlet swirl offset, in Fig. 28. For negative swirl offset the loss only increases marginally which fits with the slight increase in the hub low region at plane E. Conversely, for positive swirl offset the loss ramps up, despite the fact the duct arguably moves further from separation, which reflects the increased mixing loss generated by the larger ESS wakes. Ultimately, the results show that the ESS is more sensitive than the duct to changes in the inlet conditions. The duct itself seems to be a robust design which may be somewhat attributed to the fact it is not overly aggressive (in terms of area ratio and non-dimensional radius change). Other than an increase in loss the degradation of the flow though the rotor and ESS does not compromise the duct; it is offset by the enhanced mixing caused by the larger wake structures.

CONCLUSIONS

Experimental observations showed that a hub-low profile at inlet to the ESS had a relatively small effect on the development of the flow though the duct. An increased hub boundary layer was observed throughout, but this did not move the duct closer to separation due to the presence of a larger ESS wake structure. This promoted mixing of the higher momentum mainstream flow into the hub boundary layer thereby delaying separation. Nevertheless, the increased mixing caused the ESS/duct loss to increase by ~12% relative to a flat inlet profile.

A steady RANS CFD model employing a mixing plane between the rotor and ESS and a Reynolds Stress turbulence model achieved good agreement with the experimental data.

Increasing the boundary layer thickness at rotor inlet was observed (CFD prediction) to generate larger secondary flow structures through the rotor. Although these caused larger ESS wake structures to be observed the overall ESS/duct flow showed only small changes. The wake mixing marginally improved the low velocity flow in the critical second bend of the duct, arguably moving it further from separation but incurring a 5% further increase in loss,

Bulk swirl distortion at rotor inlet was observed (CFD prediction) to generate increased wake structures at ESS exit. For a negative shift in swirl the effect was negligible but at +10-14° the ESS were seen to develop a region of separated flow. Although generating an increase in loss of over 30% the additional mixing of the large ESS wakes again improved the low velocity flow in the critical second bend of the duct, arguably moving it further from separation.

Overall, the hub-low inlet profile and potential rotor inlet distortions appear to have limited effect on the flow at duct exit – i.e. the flow presented to the downstream compressor. The ESS may be the limiting factor in the design as it was seen to exhibit flow separation whilst the duct was not. However, the increased wake structures, and the enhanced mixing, would seem to delay separation in the duct albeit with a significant penalty in system loss.

ACKNOWLEDGMENTS

The authors would like to thank Dr Paul Denman for help with the data acquisition system and David Cooper, Neil Thorley, Tony Fardoe, Les Monk and Bill Niven for their technical assistance.

FUNDING

This research was undertaken at Loughborough University within the Rolls-Royce University Technology Centre (UTC) in Combustion System Aero Thermal Processes. It was funded by the Aerospace Technology Institute as part of the iCORE (Integrated Core Technologies) program.

NOMENCLATURE

A	Area
AR	Area Ratio
Cp	Static pressure rise coefficient, $Cp = \frac{\tilde{p}_2 - \tilde{p}_1}{\tilde{P}_1 - \tilde{p}_1}$
ESS	Engine Section Stator
h	Passage height
IGV	Inlet Guide Vane
L	Duct length
$\dot{m}$	Mass flow rate
N	Rotor speed
OGV	Outlet Guide Vane
P, p	Total, Static pressure
R_m	Mean radius
r_i	Inner wall (hub) radius
r_o	Outer wall (casing) radius
U_{blade}	Mid-height blade speed
U, V ,W	Axial, radial and tangential velocity components in cylindrical-polar coordinates
y+	Dimensionless wall distance
a	Kinetic energy flux coefficient
ρ	Density
ϕ	Rotor flow coefficient (V_{axial}/U_{blade})

ψ	Rotor work coefficient ($\Delta H/U_{blade}^2$)
θ	Flow angle
λ	Total pressure loss coefficient, $\lambda = \frac{\tilde{P}_1 - \tilde{P}_2}{\tilde{P}_1 - \tilde{p}_1}$

Superscripts

-	Area weighted spatial average
~	Mass weighted spatial average

Subscripts

L	Local coordinate system
X2, A-H	Measurement planes

REFERENCES

[1] Britchford, K. M., 1998, "The Aerodynamic Behaviour of an Annular S-Shaped Duct", Ph.D. Thesis, Loughborough University, Loughborough, UK.

[2] Bailey, D. W., 1997, "The Aerodynamic Performance of an Annular S-shaped Duct", Ph.D. Thesis, Loughborough University, Loughborough, UK.

[3] Britchford, K. M., Manners, A. P., McGuirk, J. J. and Stephens, S. J., 1993, "Measurements and Prediction of Flow in Annular S-Shaped Ducts", Proceedings of the Second International Symposium on Engineering Turbulence Models and Measurements, Florence, Italy, May 31 – June 2, pp. 785-794.

[4] Britchford, K.M., Carrotte, J.F., Stevens, S.J. and McGuirk, J.J., 1994, "The Development of the Mean Flow and Turbulence Structure in an Annular S-Shaped Duct", Proceeding of ASME Turbo Expo, The Hague, Netherlands, June 13-16, 1994, ASME Paper No. 94-GT-457.

[5] Britchford, K. M., Carrotte, J. F., Kim, J. H. and Hield, P. M., 2001, "The Effect of Operating Conditions on the Aerodynamic Performance of an Integrated OGV S-Shaped Duct", Proceeding of ASME Turbo Expo, New Orleans, USA, June 4-7, 2001, ASME Paper No. 2001-GT-0347.

[6] Bailey, D.W. and Carrotte, J.F., 1996, "The Influence of Inlet Swirl on the Flow within an Annular S-Shaped Duct", Proceeding of ASME Turbo Expo, Birmingham, UK, June 10-13, 1996, ASME Paper No. 96-GT-60.

[7] Bailey, D. W., Britchford, K. M., Carrotte, J. F. and Stevens, S. J., 1997, "Performance Assessment of an Annular S-Shaped Duct", ASME J. of Turbomach., 119(1), pp 149-156, doi.org/10.1115/1.2841003.

[8] Ortiz-Duenas, C., Miller, R. J., Hodson, H. P., and Longley, J. P., 2007, "Effect of Length on Compressor Inter-Stage Duct Performance", Proceeding of ASME Turbo Expo, Montreal, Canada, May 14-17, 2007, ASME Paper No. GT2007-27752.

[9] Barker, A. G., Carrotte, J. F. and Walker, A. D., 2005, "Aggressive Intermediate Duct Aerodynamics, Deliverable 1.20.1: Interim Report on LU1 Test Results", AIDA, EU Contract FP6-AST3-CT-2003-502836, Dept. Aeronautical and Automotive Engineering, Loughborough University, UK.

[10] Barker, A. G., Carrotte, J. F. and Walker, A. D., 2006, "Aggressive Intermediate Duct Aerodynamics, Deliverable 1.20.2: Final Report on LU1 Test/CFD Results", AIDA, EU Contract FP6-AST3-CT-2003-502836, Dept. Aeronautical and Automotive Engineering, Loughborough University, UK.

[11] Karakasis, M. K., Naylor, E. M. J., Miller, R. J., and Hodson, H. P., 2010, "The Effect of an Upstream Compressor on a Non-Axisymmetric S-Duct", Proceeding of ASME Turbo Expo, Orlando, USA, June 8-12, 2010, ASME Paper No. GT2010-23404.

[12] Walker, A.D., Barker, A.G. and Carrotte, J.F., 2011, "Numerical Design and Experimental Evaluation of an Aggressive S-shaped Compressor Transition Duct with Bleed", Proceeding of ASME Turbo Expo, Vancouver, Canada, June 11-15, 2011, ASME Paper No. GT2011-45628.

[13] Walker, A.D., Barker, A.G., Carrotte, J.F., Bolger, J.J. and Green, M.J., 2013, "Integrated OGV Design for an Aggressive S-shaped Compressor Transition Duct", . Turbomach., 135(1), 011035, doi.org/10.1115/1.4006331.

[14] Walker, A.D., Barker, A.G., Mariah, I., Peacock, G.L., Carrotte, J.F., and Northall, R.M., 2014, "An Aggressive S-Shaped Compressor Transition Duct with Swirling Flow and Aerodynamically Lifting Struts", Proceeding of ASME Turbo Expo, Dusseldorf, Germany, June 16-20, 2014, ASME Paper No. GT2014-25844.

[15] Zamboni, G., and Xu, L., 2012, "Fan Root Aerodynamics for Large Bypass Gas Turbine Engines: Influence on the Engine Performance and 3D Design", J. Turbomach., 134(6): 061017, doi.org/10.1115/1.4006286.

[16] Peters, A., Spakovszky, S.S., Wesley, K., and Rose, B., 2015, "Ultrashort Nacelles for Low Pressure Ratio Propulsors", J. Turbomach., 137(2): 021001. doi.org/10.1115/1.4028235.

[17] Cumpsty, N. A., 1989, "Compressor Aerodynamics", Longman Scientific and Technical, Harlow, Essex, UK.

[18] Wray, A. P. and Carrotte, J. F., 1993, "The Development of a Large Annular Facility for Testing Gas Turbine Combustor Diffuser Systems", Proceedings of the 29th Joint Propulsion Conference and Exhibit, Monterey, USA, June 28-30, 1993, Paper No, AIAA-93-2546.

[19] Klein, A., 1995, "Characteristics of Combustor Diffusers", Prog. Aerosp. Sci., 31(3), pp. 171-271, doi.org/10.1016/0376-0421(95)00006-K.

Journal of Turbomachinery. Received September 09, 2019;
Accepted manuscript posted October 17, 2019. doi:10.1115/1.4045272

Figure Captions List

Journal of Turbomachinery. Received September 09, 2019;
Accepted manuscript posted October 17, 2019. doi:10.1115/1.4045272

Fig. 1 Static pressure in an S-shaped duct [14]

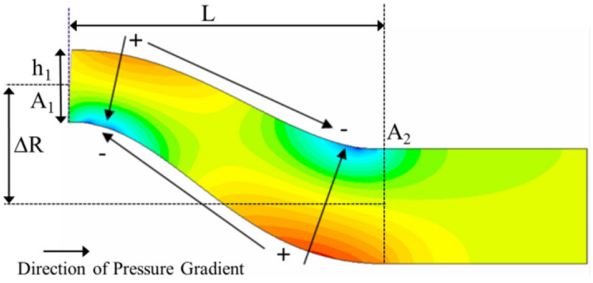

Journal of Turbomachinery. Received September 09, 2019;
Accepted manuscript posted October 17, 2019. doi:10.1115/1.4045272

Fig. 2 Schematic of the compression system in a high bypass ratio turbofan

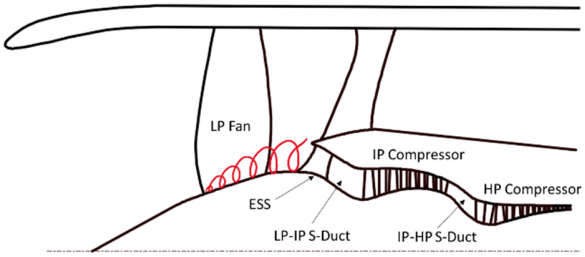

Journal of Turbomachinery. Received September 09, 2019;
Accepted manuscript posted October 17, 2019. doi:10.1115/1.4045272

Fig. 3 Schematic of iCORE duct

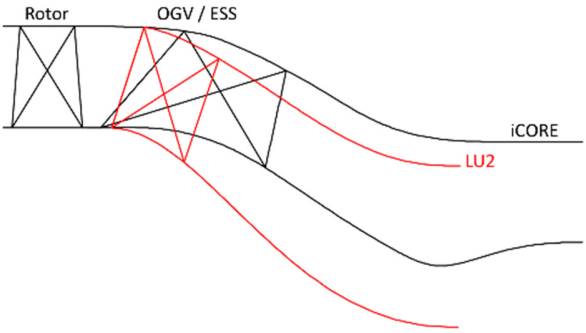

	L/h_1	$\Delta R/L$	A_2/A_1
LU2	3.1	0.5	1.0
iCORE	3.3	0.4	0.9

Fig. 4 Test facility schematic

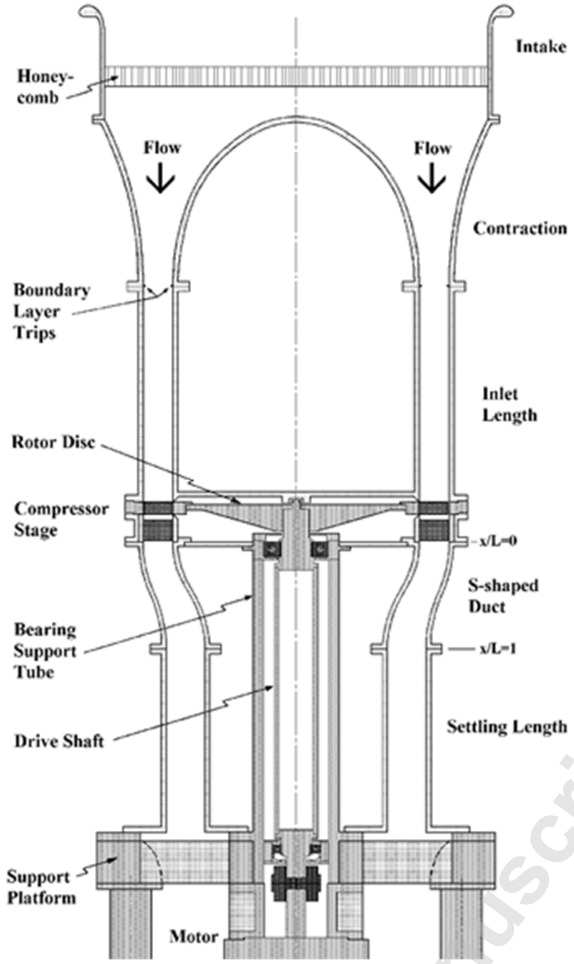

Journal of Turbomachinery. Received September 09, 2019;
Accepted manuscript posted October 17, 2019. doi:10.1115/1.4045272

Fig. 5 Traverse planes

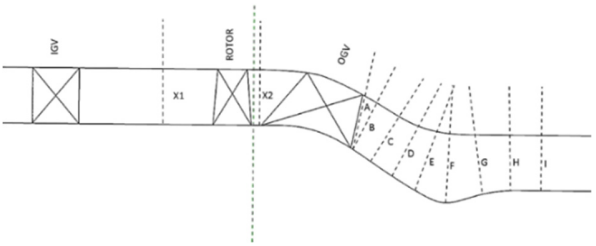

Journal of Turbomachinery. Received September 09, 2019;
Accepted manuscript posted October 17, 2019. doi:10.1115/1.4045272

Fig. 6 Local coordinate system

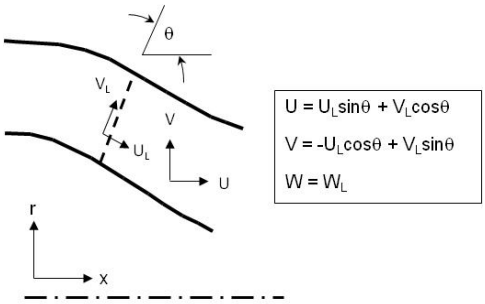

Fig. 7 Normal velocity contours at rotor exit (X2): (a) phase 1, (b) phase 2

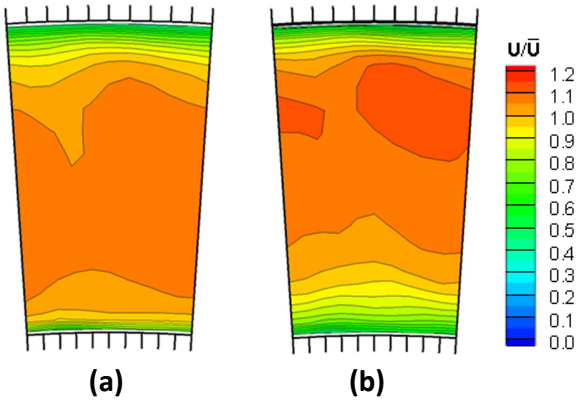

Journal of Turbomachinery. Received September 09, 2019;
Accepted manuscript posted October 17, 2019. doi:10.1115/1.4045272

Fig. 8 Circumferentially averaged radial profiles at rotor exit (X2)

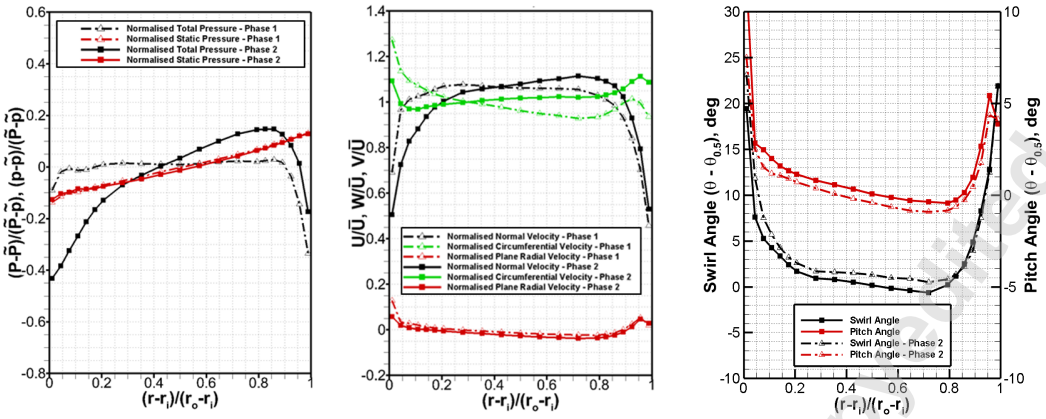

Fig. 9 Normal velocity contours at ESS exit (A): (a) phase 1 (b) phase 2

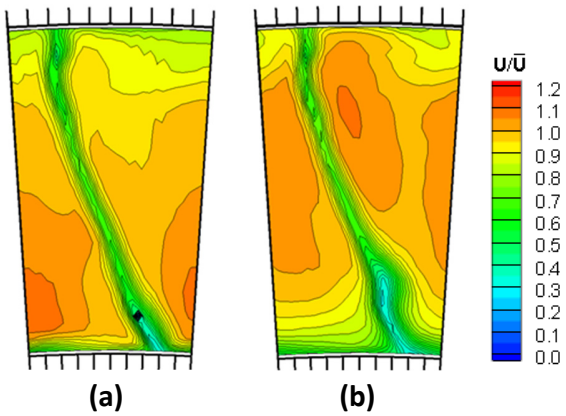

Journal of Turbomachinery. Received September 09, 2019;
Accepted manuscript posted October 17, 2019. doi:10.1115/1.4045272

Fig. 10 Circumferentially averaged radial profiles at ESS exit (A)

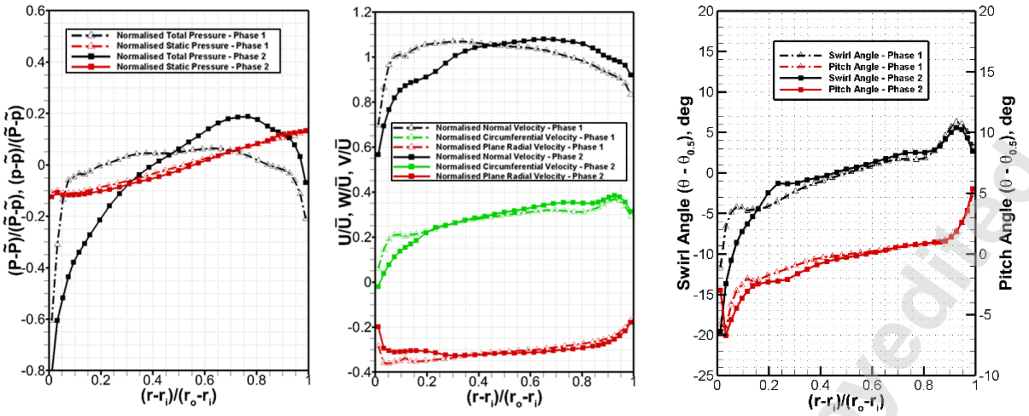

Journal of Turbomachinery. Received September 09, 2019;
Accepted manuscript posted October 17, 2019. doi:10.1115/1.4045272

Fig. 11 Circumferentially averaged radial profiles

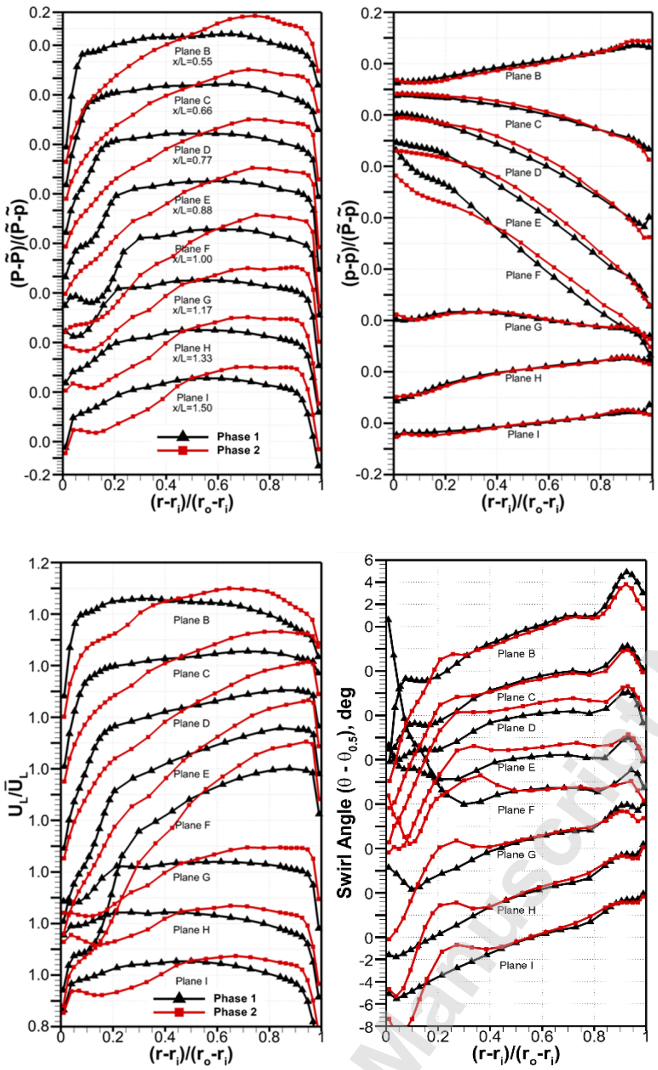

Journal of Turbomachinery. Received September 09, 2019;
Accepted manuscript posted October 17, 2019. doi:10.1115/1.4045272

Fig. 12 Flow development - normal velocity contours: (a) phase 1, (b) phase 2

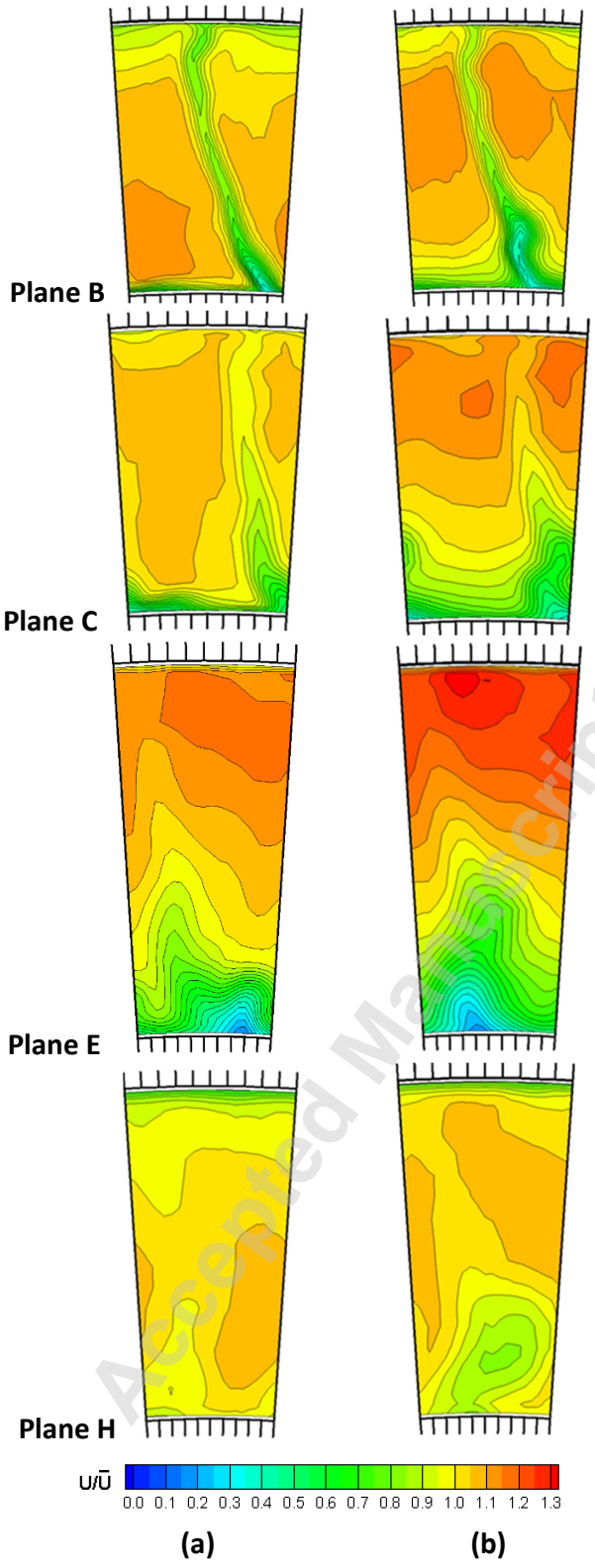

Journal of Turbomachinery. Received September 09, 2019;
Accepted manuscript posted October 17, 2019. doi:10.1115/1.4045272

Fig. 13 Comparison of total pressure loss coefficient

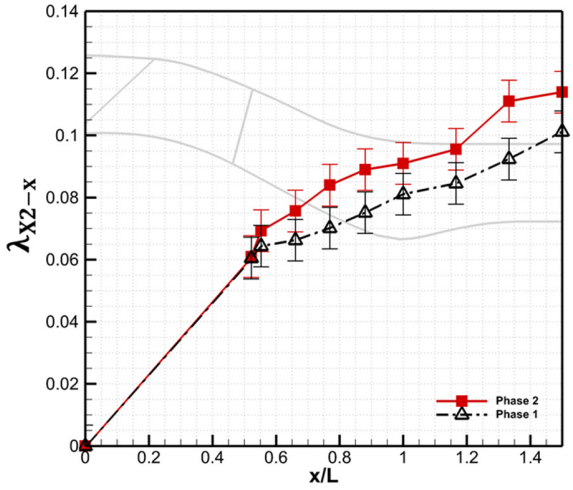

Journal of Turbomachinery. Received September 09, 2019;
Accepted manuscript posted October 17, 2019. doi:10.1115/1.4045272

Fig. 14 CFD validation – rotor exit (X)

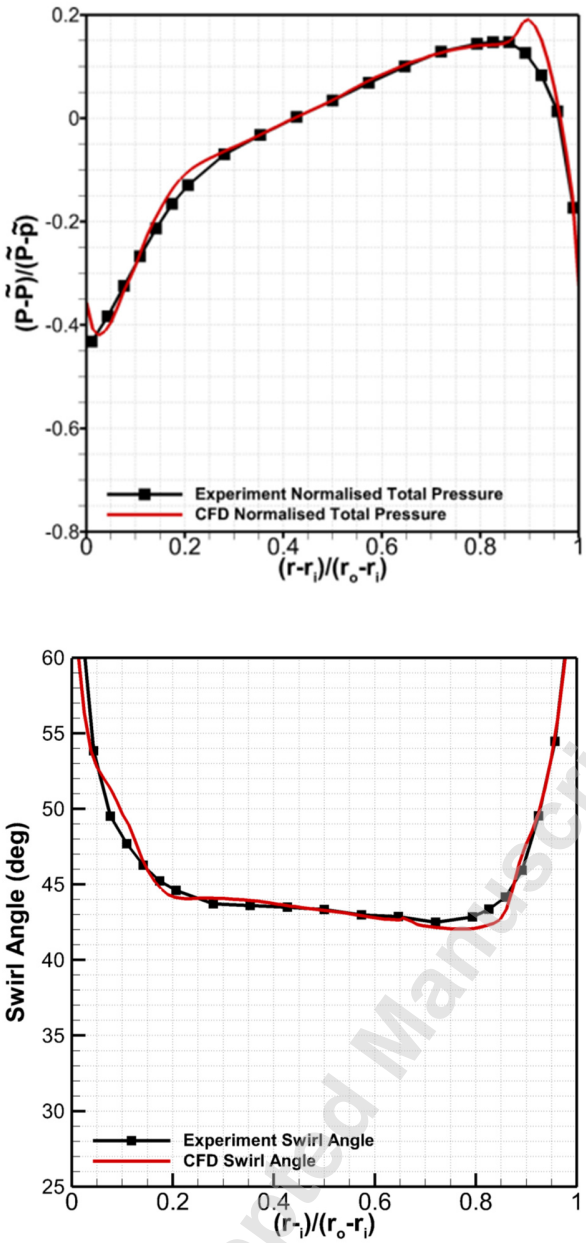

Fig. 15 Predicted normal velocity contours – phase 2

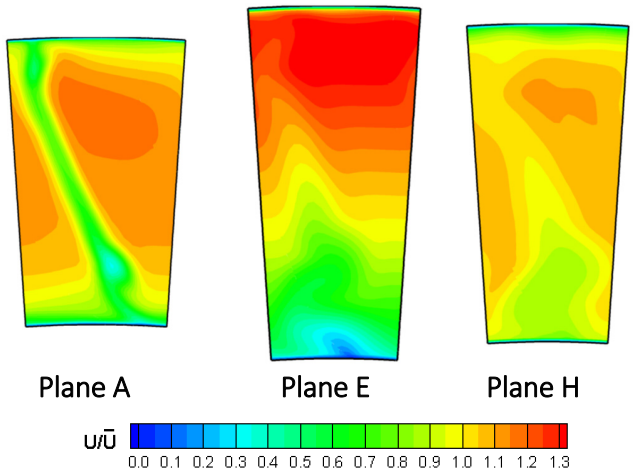

Fig. 16 Comparison of total pressure loss coefficient (Exp. V CFD) – phase 2

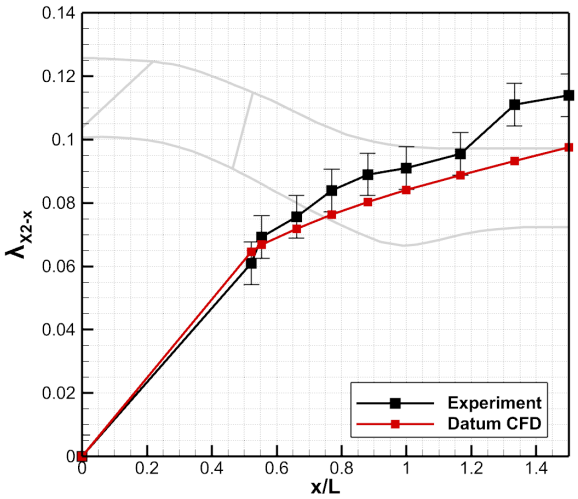

Journal of Turbomachinery. Received September 09, 2019;
Accepted manuscript posted October 17, 2019. doi:10.1115/1.4045272

Fig. 17 Rotor inlet profile

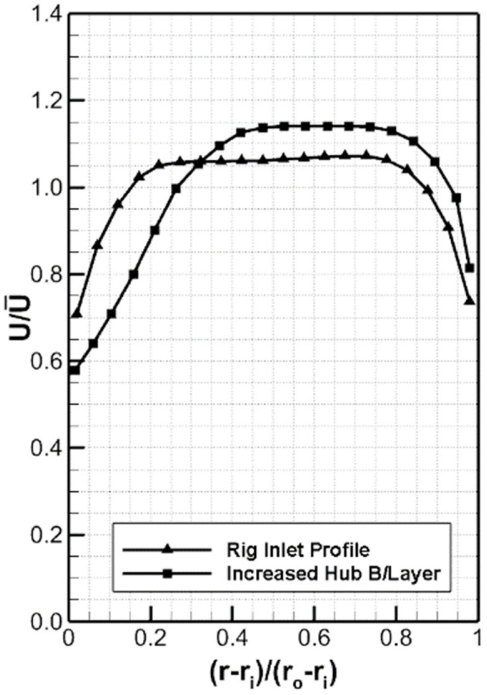

Fig. 18 Predicted normal velocity contours at rotor exit (X2) – rotating frame: (a) rig inlet, (b) increased hub boundary layer

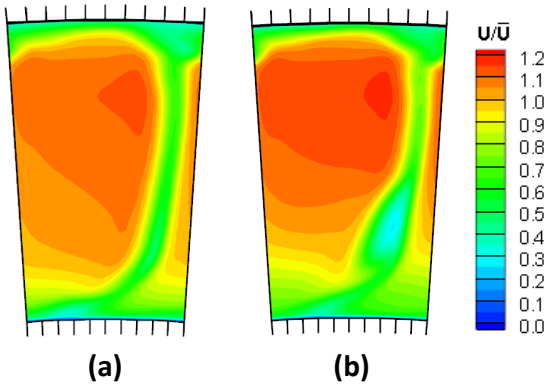

Journal of Turbomachinery. Received September 09, 2019;
Accepted manuscript posted October 17, 2019. doi:10.1115/1.4045272

Fig. 19 Predicted normal velocity contours at ESS exit (A): (a) rig inlet, (b) increased hub boundary layer

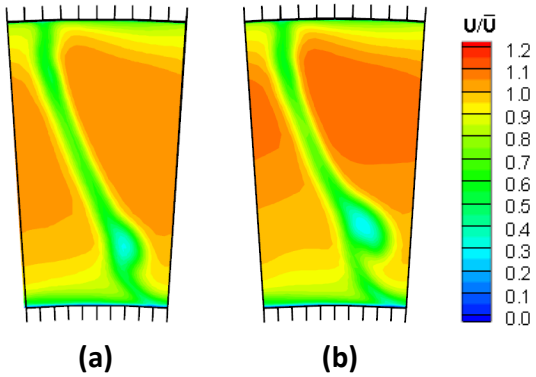

Fig. 20 Predicted normal velocity contours at plane E: (a) rig inlet, (b) increased hub boundary layer

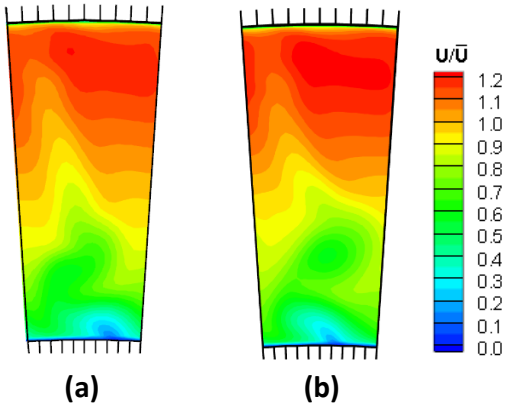

Fig. 21 Predicted normal velocity contours at Plane H: (a) rig inlet, (b) increased hub boundary layer

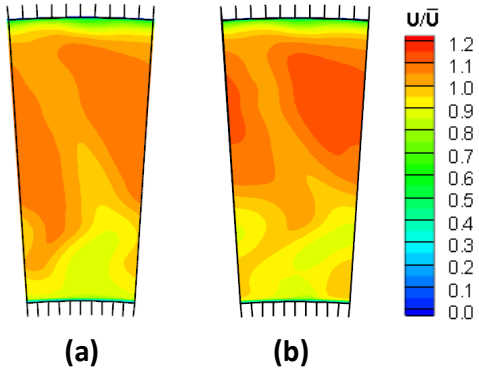

Journal of Turbomachinery. Received September 09, 2019;
Accepted manuscript posted October 17, 2019. doi:10.1115/1.4045272

Fig. 22 Comparison of total pressure loss coefficient

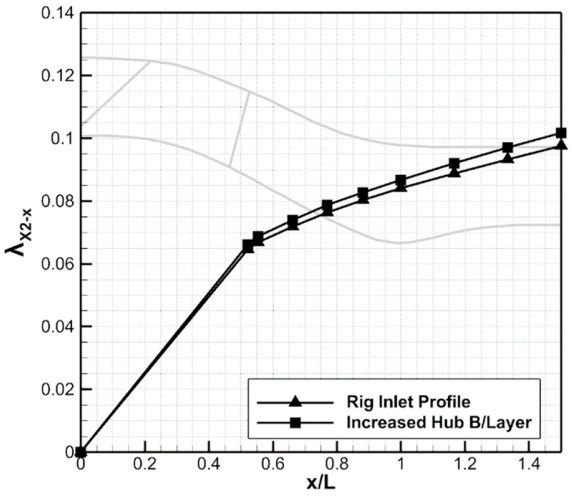

Journal of Turbomachinery. Received September 09, 2019;
Accepted manuscript posted October 17, 2019. doi:10.1115/1.4045272

Fig. 23 Predicted rotor exit (X2) swirl profile

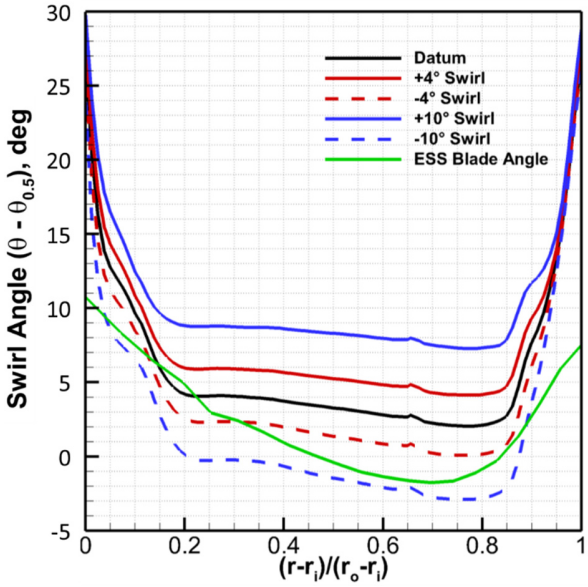

Journal of Turbomachinery. Received September 09, 2019;
Accepted manuscript posted October 17, 2019. doi:10.1115/1.4045272

Fig. 24 Predicted normal velocity contours at ESS exit (A)

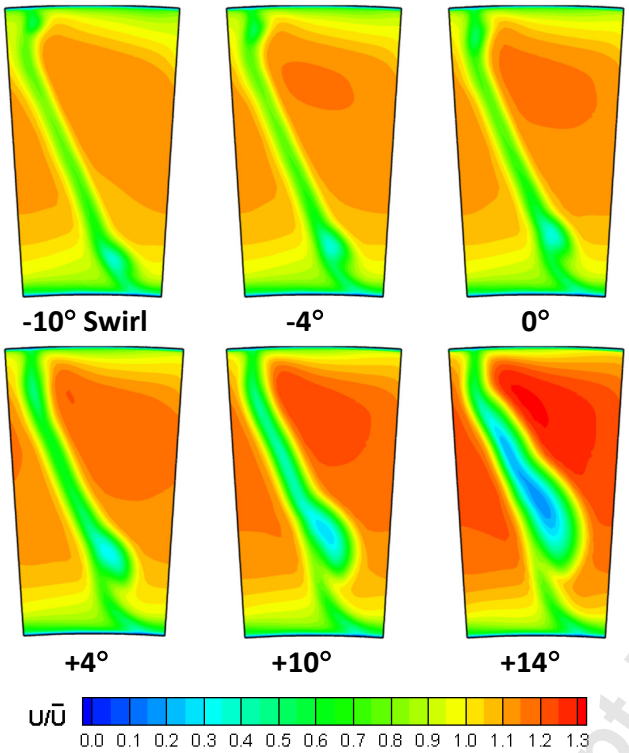

Journal of Turbomachinery. Received September 09, 2019;
Accepted manuscript posted October 17, 2019. doi:10.1115/1.4045272

Fig. 25 ESS surface streamlines

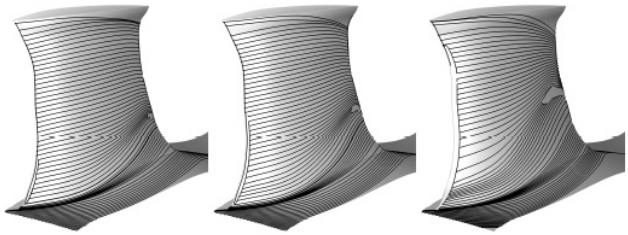

Journal of Turbomachinery. Received September 09, 2019;
Accepted manuscript posted October 17, 2019. doi:10.1115/1.4045272

Fig. 26 Predicted normal velocity contours at plane E

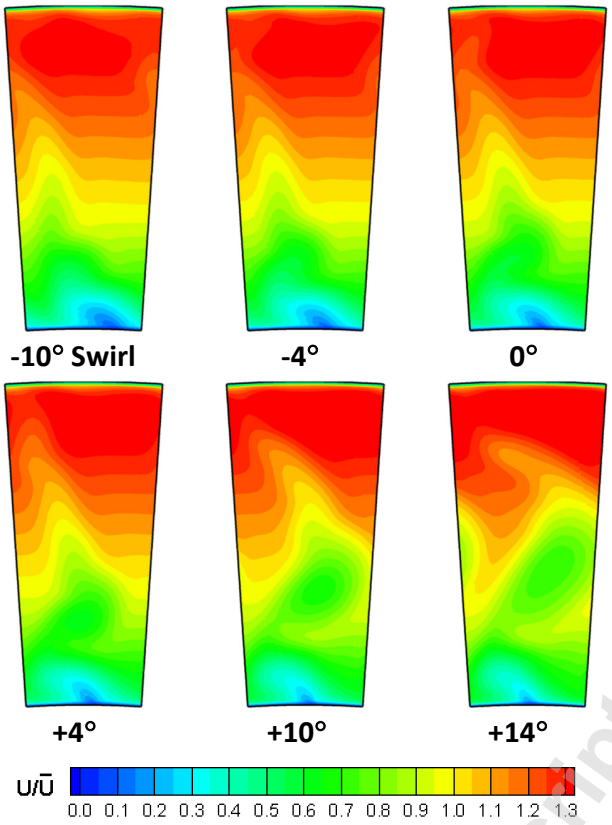

Journal of Turbomachinery. Received September 09, 2019;
Accepted manuscript posted October 17, 2019. doi:10.1115/1.4045272

Fig. 27 Predicted normal velocity contours at plane H

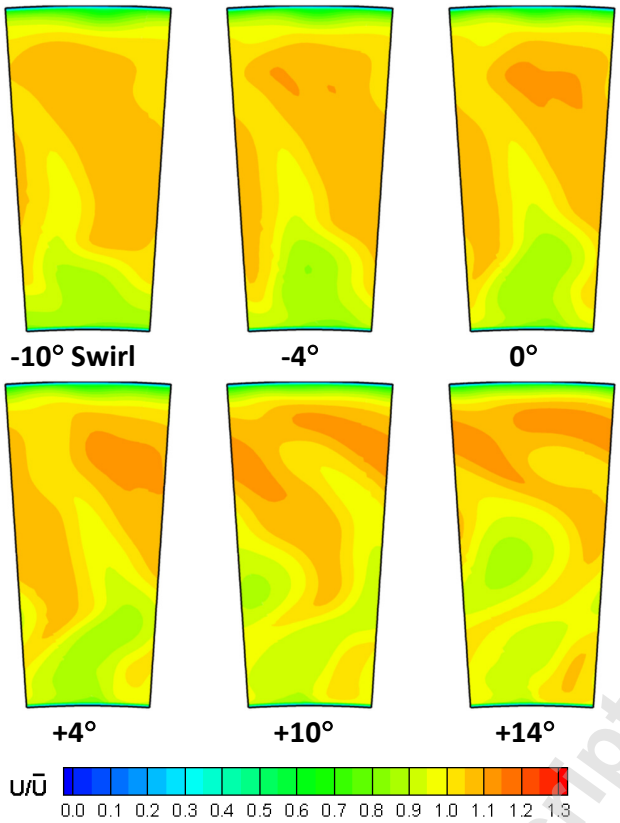

Journal of Turbomachinery. Received September 09, 2019;
Accepted manuscript posted October 17, 2019. doi:10.1115/1.4045272

Fig. 28 Effect of inlet swirl on total pressure loss